

# Lagrangian Coherent Structure Analysis of Terminal Winds Detected by Lidar. Part I: Turbulence Structures

WENBO TANG

*School of Mathematical and Statistical Sciences, Arizona State University, Tempe, Arizona*

PAK WAI CHAN

*Hong Kong Observatory, Hong Kong, China*

GEORGE HALLER

*Department of Mechanical Engineering, and Department of Mathematics and Statistics, McGill University, Montreal, Quebec, Canada*

(Manuscript received 10 March 2010, in final form 9 September 2010)

## ABSTRACT

The accurate real-time detection of turbulent airflow patterns near airports is important for safety and comfort in commercial aviation. In this paper, a method is developed to identify Lagrangian coherent structures (LCS) from horizontal lidar scans at Hong Kong International Airport (HKIA) in China. LCS are distinguished frame-independent material structures that create localized attraction, repulsion, or high shear of nearby trajectories in the flow. As such, they are the fundamental structures behind airflow patterns such as updrafts, downdrafts, and wind shear. Based on a recently developed finite-domain–finite-time Lyapunov exponent (FDFTLE) algorithm from Tang et al. and on new Lagrangian diagnostics presented in this paper that are pertinent to the extracted FDFTLE ridges, the authors differentiate LCS extracted from lidar data. It is found that these LCS derived from horizontal lidar scans compare well to convergence and divergence suggested by vertical slice scans. At HKIA, horizontal scans are predominant: they cover much bigger azimuthal ranges as compared with only two azimuthal angles from the vertical scans. LCS extracted from horizontal scans are thus advantageous in providing organizing turbulence structures over the entire observational domain as compared with a single line along the vertical scan direction. In Part II of this study, the authors will analyze the evolution of LCS and their impacts on landing aircraft based on recorded flight data.

## 1. Introduction

Airplane wakes, terrain-disrupted airflows, sea breeze, gust fronts, and microbursts often create significant low-altitude wind shear. Such wind shear is an aviation hazard as it may change the lift on the aircraft and lead to instability. Real-time detection of low-altitude, shear-inducing flow structures is, therefore, a major challenge in aviation safety.

In this paper, we introduce a new methodology that addresses the above challenge. Specifically, we use the recently developed finite-domain–finite-time Lyapunov exponent (FDFTLE) method (Tang et al. 2010a) to extract

low-altitude flow structures from terminal winds over Hong Kong International Airport (HKIA) in China. We also provide a suite of mathematical tools developed to differentiate the types of flow structures extracted from the FDFTLE method.

Traditionally, real-time monitoring of terminal winds is provided through Terminal Doppler Wind Radars (TDWR). These are remote sensing systems developed for humid weather, as raindrops are necessary for the velocity measurement they provide. Recently, coherent Doppler Light Detection and Ranging (lidar) systems have been developed and implemented at several major airports in Asia, Europe, and North America for the detection of wake vortices caused by jumbo jets and nearby terrains in dry weather.

Both radar and lidar systems output line-of-sight (LOS) velocity, or radial velocity of the wind field with respect to the sensor. These outputs provide important yet partial

---

*Corresponding author address:* Wenbo Tang, School of Mathematical and Statistical Sciences, Arizona State University, Tempe, AZ 85287.

E-mail: wenbo.tang@asu.edu

information of the flow field, such as the headwind profile along runway corridors.

To better reveal the airflow structure, variational wind retrieval techniques have been developed to estimate the flow fields based on conical scans at different elevation angles (Sun et al. 1991; Qiu and Xu 1992; Qiu et al. 2006; Chan and Shao 2007). The retrieval yields two- or three-dimensional velocity data, depending on the particular scheme chosen. Discussion on the turbulent structure of real-time terminal winds involves primarily Eulerian descriptions derived from instantaneous snapshots of the retrieved wind velocity.

It has recently been broadly recognized that Eulerian (i.e., purely velocity-field-based) descriptions of an unsteady flow field have inherent flaws, as instantaneous streamlines or various velocity derivatives do not provide an objective representation of actual *particle motion* in a time-dependent flow (Jeong and Hussain 1995; Haller 2005).

By contrast, Lagrangian (i.e., particle based) analysis is a frame-independent way of locating flow structures in air particle motion. Specifically, finite-time Lyapunov exponents computed on fluid trajectories can be used to locate Lagrangian coherent structures (LCS) that attract or repel nearby trajectories at locally the highest rate in the flow (Haller 2001). FTLE analysis has been implemented in a number of studies on geophysical flow structures in two- and three-dimensional velocity fields. (Lekien et al. 2005; Coulliette et al. 2007; Tang et al. 2010b). Observational velocity data are, however, inherently limited in space because of range limitations of remote sensing systems. At the same time, Lagrangian methods quantifying separation and attraction require long-term integration, and hence velocity data on extended domains.

In the absence of large-scale velocity observations, Lagrangian fluid trajectory integration has traditionally been stopped at the boundary of the observational domain. This practice turns the observational boundaries into attractors (i.e., spurious attractive LCS). Furthermore, different boundary components (e.g., two orthogonal sides of a rectangular boundary) will act as separate attractors, creating yet another spurious structure—a separatrix (or repelling LCS) between the two domains of attraction. Such spurious structures can be so pronounced that they actually overshadow the true LCS on the corresponding finite-time Lyapunov exponent plots.

To circumvent the above problems, we employ the above-mentioned FDFTLE technique (Tang et al. 2010a) to lidar retrieval data from Hong Kong International Airport. HKIA is situated in the vicinity of Lantau Island, which has mountain peaks up to almost 1 km above mean sea level (MSL) and valleys of around 400 m MSL in between. The majority of wind shear at HKIA occurs in clear weather as terrain-induced turbulence generated at

its mountainous neighbor (Chan and Shao 2007). Because of the presence of these terrain-disrupted flows, real-time reports of turbulence structures around the airport have proved to be a challenge.

We analyze three turbulent flow cases under different weather conditions between April 2008 and February 2009. In these cases, lidar conical scans at two elevation angles are available at roughly 150-s intervals. They are used to generate the two-dimensional retrieved wind fields. FDFTLE analysis is then performed by integrating fluid particle trajectories in forward and backward time using the wind fields and evaluating the FTLE along Lagrangian trajectories. LCS are extracted as maximum ridges of the forward- and backward-time FDFTLE fields. We then compare the extracted LCS with features in vertical slice scans to infer the full three-dimensional structures near ground.

The rest of the paper is outlined as follows: in section 2 we discuss typical terrain-induced turbulence structures experienced at HKIA, the lidar systems, and the wind retrieval technique used in this study. In section 3 we summarize the FDFTLE method from Tang et al. (2010a). In section 4 we discuss the additional mathematical tools developed to differentiate the flow structures. In section 5 we identify flow structures under different weather conditions from the HKIA data. In section 6, we draw conclusions and discuss further studies that are under way.

In Tang et al. (2011, manuscript submitted to *J. Appl. Meteor. Climatol.*, hereinafter Part II), we will analyze specific landing attempts during the observational periods discussed in this paper. Our analyses indicate a strong correlation between the LCS we extract and the jitters experienced by landing aircraft.

## 2. Characteristics of wind disturbances, remote sensing, and wind retrieval at HKIA

Owing to its proximity to Lantau Island and other mountains surrounding the airport, the majority of turbulent structures at HKIA are terrain induced. Given the length scale of the nearby terrain and typical wind conditions, these structures are generally found to be small sized, with the horizontal dimensions as small as several hundred meters. After generation, they could be advected with the background wind and affect a runway corridor in a short time interval.

In a typical wind of  $20 \text{ m s}^{-1}$ , a turbulent patch of length scale 500 m will traverse the runway corridor in just 25 s. It takes even less time for an airplane to traverse the turbulent patch because of its approach speed. Turbulence structures could lose their coherence in a short time as well, as they drift over the runway and eventually dissipate

(Chan and Shun 2005). Therefore, the wind shear experienced by aircraft is transient and sporadic in nature.

For wind monitoring in dry weather at HKIA, two coherent Doppler lidars are operated by the Hong Kong Observatory (HKO). Each lidar operates at a wavelength of 2 microns with pulse energy of about 2 mJ. The pulse repetition frequency is 500 Hz and line-of-sight data are output at 10 Hz (i.e., an average of 50 pulses for each datum). The range resolution is about 100 m; the measurement distance starts from about 400 m and is up to 10 km. The maximum unambiguous velocity is normally  $20 \text{ m s}^{-1}$ , extendable to  $40 \text{ m s}^{-1}$  at the expense of the range.

To reveal the most important coherent structures impacting flights, the lidar systems at HKIA have employed a special scan strategy, comprising the following scans:

- 1) plan position indicator (PPI) scans (or conical scans) provide the weather forecasters with an overview of the wind condition in the vicinity of HKIA. PPI scans at  $1.4^\circ$ ,  $3.0^\circ$ , and  $6.0^\circ$  are implemented for the northern lidar and those at  $3.2^\circ$  and  $6.0^\circ$  are implemented for the southern lidar. The first two scans of the northern lidar are used in this study, as they are closer to the angle of

approach. The PPI scans are blocked by the tower of the fire stations to the north. Moreover, because of the close proximity to residential areas on Lantau Island and the low PPI angle, as a laser safety measure, sector blanking has been applied for the residential area outside HKIA.

- 2) range–height indicator (RHI) scans (or vertical slice scans) measure the vertical structure of the wind shear features (e.g., interaction between sea breeze and the background flow, hydraulic jump in cross-mountain airflow, etc.).
- 3) glide-path scans focus on the wind conditions along the glide paths for operational wind shear alerting—the lidar estimates the headwind profile to be encountered by the aircraft and significant wind changes in the profile are detected automatically (Shun and Chan 2008).

Because the HKIA lidars are in operational use, we only work with datasets obtained from existing scanning strategy and compare our results with standard lidar products at HKO.

The 2D wind retrieval algorithm for lidar is modified from a two-step variational method for radar (Qiu et al. 2006). The cost function  $J$  to be minimized is given by

$$\begin{aligned}
 J(u, v) &= J_1 + J_2 + J_3 + J_4 + J_5 + J_6 \\
 &= \sum_{i,j} \left\{ W_1 [(u - u_B)^2 + (v - v_B)^2] + W_2 (v_r - v_r^{\text{obs}})^2 + W_3 (\Delta x)^2 + W_4 (\Delta x)^2 \left( \frac{\partial v}{\partial x} + \frac{\partial u}{\partial y} \right)^2 \right. \\
 &\quad \left. + W_5 (\Delta x)^4 (\nabla^2 u + \nabla^2 v) + \sum_n \left[ W_6 \left( \frac{\partial v_r^{\text{obs}}}{\partial t} + u \frac{\partial v_r^{\text{obs}}}{\partial x} + v \frac{\partial v_r^{\text{obs}}}{\partial y} \right)^2 \right] \right\}, \tag{1}
 \end{aligned}$$

where  $u$  and  $v$  are the components of the retrieved wind field, subscript  $B$  is the background field generated from lidar radial velocity in the way described in Qiu et al. (2006),  $v_r$  is the retrieved radial velocity, superscript obs denotes the observed values,  $i$  and  $j$  define the horizontal grid point, and  $n$  is the time index (three consecutive scans are used in each analysis). The weights are  $W_1 = 0.1$  (after the first step retrieval),  $W_2 = 1$ ,  $W_3 = W_4 = W_5 = 0.1$ , and  $W_6 = 10^4$ . They are chosen empirically in this paper to ensure that the constraints have proper orders of magnitude. Compared to Qiu et al. (2006), Eq. (1) has two new terms, namely,  $J_5$  and  $J_6$ , and does not consider those terms that are related to precipitation and mass conservation. The role of  $J_5$  is mainly for smoothing the retrieved wind field;  $J_6$  aims at ensuring a kind of conservation of the momentum associated with the observed radial velocity. With this approach, it is hoped that the retrieved velocity field would also observe conservation of momentum approximately.

Before performing the retrieval, the radial velocity data are quality controlled to remove the outliers due to,

for instance, reflection from clutters. The main source of clutter is the moving aircraft in the sky and the clutter does not occur very frequently (on the order of a few per day). Such outliers could be detected by setting a threshold of signal-to-noise ratio and comparing the difference of radial velocity from adjacent range gates; they are then replaced by a median-filtered value determined from neighboring range gates. Finally, the quality-controlled radial velocity in the range–azimuth coordinate system is interpolated to a Cartesian grid with a resolution of 100 m using Barnes' scheme.

Figure 1a shows a typical lidar output. The color map indicates the LOS velocity, with positive values denoting motion away and negative values denoting motion toward the lidar. Sector blanking and tower blockage are apparent in this figure. Also note that since the lidar is scanning at  $1.4^\circ$  the light beams cannot penetrate the mountains; hence there is poor data coverage south of the airport. The white contours indicate constant elevation of the terrain near the airport at 100-m intervals. The two runway strips are also shown as white rectangles in the center of the plot, with

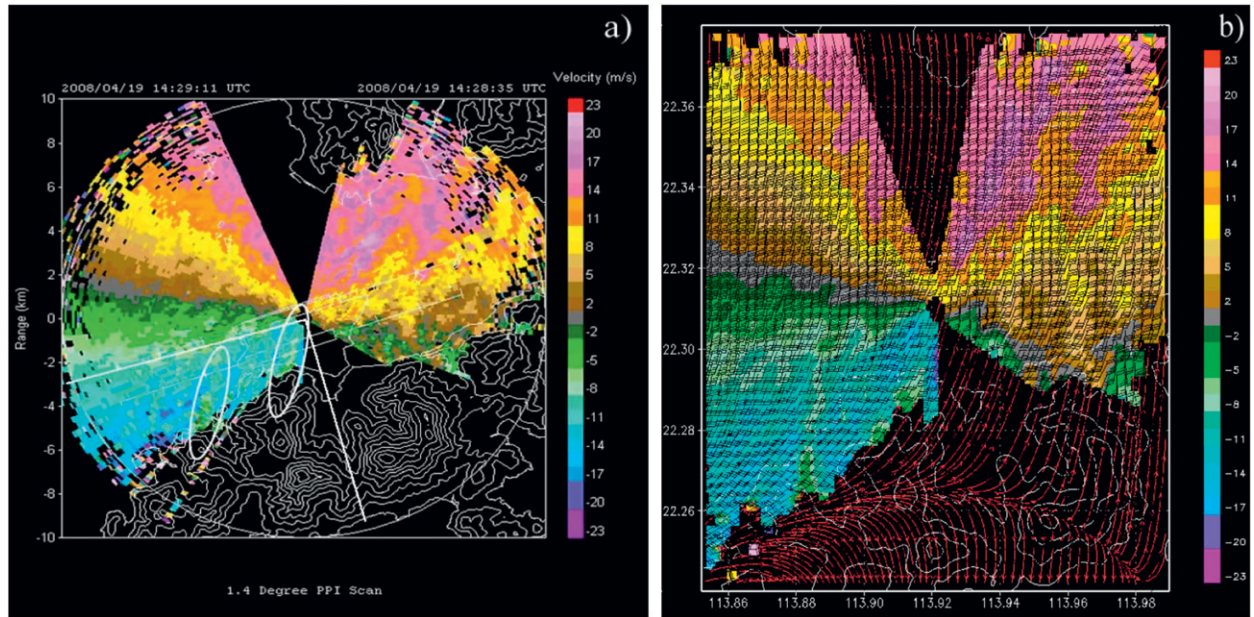


FIG. 1. (a) LOS velocity measured by the northern lidar at 1429 UTC 19 Apr 2008, superimposed with contour plot of the terrain, runway strips, and RHI scan directions. Positive values indicate LOS velocity away from lidar. The two white ellipses mark LOS anomalies that generated flow structures in later discussions. Axes are kilometers from the lidar. (b) Wind vectors and streamlines based on the retrieved velocity at the same time as (a). Axes are longitude and latitude.

runway corridors marked at the ends of the runways and tick marks at 1, 2, and 3 nm away from the runway ends.

Two RHI scans performed by the northern lidar ( $22.313^{\circ}\text{N}$ ,  $113.92^{\circ}\text{E}$ ), at  $258^{\circ}$  azimuth along the runway corridor and at  $163^{\circ}$  into a mountain gap, are shown as white thick lines. The two white ellipses mark terrain-induced flow structures, which will be discussed in section 5. Figure 1b shows streamlines and wind vectors generated from the retrieved wind field. Note that this is the standard wind retrieval output being used at HKO. Wind velocities in the blocked regions are obtained with the retrieval technique. Retrieved velocities in the unresolved regions south of HKIA are most uncertain; and they are not taken into consideration in the Lagrangian integration in the FDFTLTLE analyses. These data can be treated roughly as horizontal wind velocities near the surface of the terrain. From these figures, one can only infer a few features having “streaks” that originate from the terrain.

### 3. The FDFTLTLE algorithm

Here we summarize the finite-domain–finite-time Lyapunov exponent algorithm from Tang et al. (2010a). The FDFTLTLE algorithm is performed in two steps. First, assume that a velocity field  $\mathbf{u}(\mathbf{x}, t)$  is known over a Cartesian grid  $\mathcal{G}$  in a rectangular region, where the coordinate axes have been chosen such that the domain center corresponds to the origin. The closest linear incompressible

flow that minimizes error in the Euclidean norm is given as

$$\mathbf{v}_L(\mathbf{x}, t) = \begin{pmatrix} \frac{\langle xu_1 - yu_2 \rangle}{\langle x^2 + y^2 \rangle} & \frac{\langle yu_1 \rangle}{\langle y^2 \rangle} \\ \frac{\langle xu_2 \rangle}{\langle x^2 \rangle} & \frac{\langle yu_2 - xu_1 \rangle}{\langle x^2 + y^2 \rangle} \end{pmatrix} \mathbf{x} + \begin{pmatrix} \langle u_1 \rangle \\ \langle u_2 \rangle \end{pmatrix}. \quad (2)$$

{Here  $\langle g \rangle = [\sum_{i=1}^m \sum_{j=1}^n g(x_i, y_j)] / (m \times n)$  is the spatial average of a function  $g$  over the grid  $\mathcal{G}$ .}

The global flow is constructed on the whole plane by letting

$$\mathbf{v} = \mathbf{v}_L + (\mathbf{u} - \mathbf{v}_L)f, \quad (3)$$

where  $f$  is a filter function that takes a value of 1 inside a subset  $\mathcal{G}^0$  of  $\mathcal{G}$  and value 0 in the exterior of  $\mathcal{G}$ . Between we have a buffer zone of width  $\Delta$ , where  $f$  smoothly transitions between 1 and 0. This allows a smooth transition between the velocity fields inside  $\mathcal{G}^0$  and outside  $\mathcal{G}$ . As such, trajectory integration from the global velocity  $\mathbf{v}$  will also be smooth. Details of a filter function on a rectangular domain are discussed in Tang et al. (2010a). In this paper, as we will discuss in section 4, the filter function is modified slightly to exclude some spurious data (cf. Fig. 2). With the above extension, we have

$$\mathbf{v}(\mathbf{x}, t) = \begin{cases} \mathbf{u}(\mathbf{x}, t), & \mathbf{x} \in \mathcal{G}^0 \\ \mathbf{v}_L(\mathbf{x}, t), & \mathbf{x} \notin \text{interior}(\partial\mathcal{G}) \end{cases}. \quad (4)$$

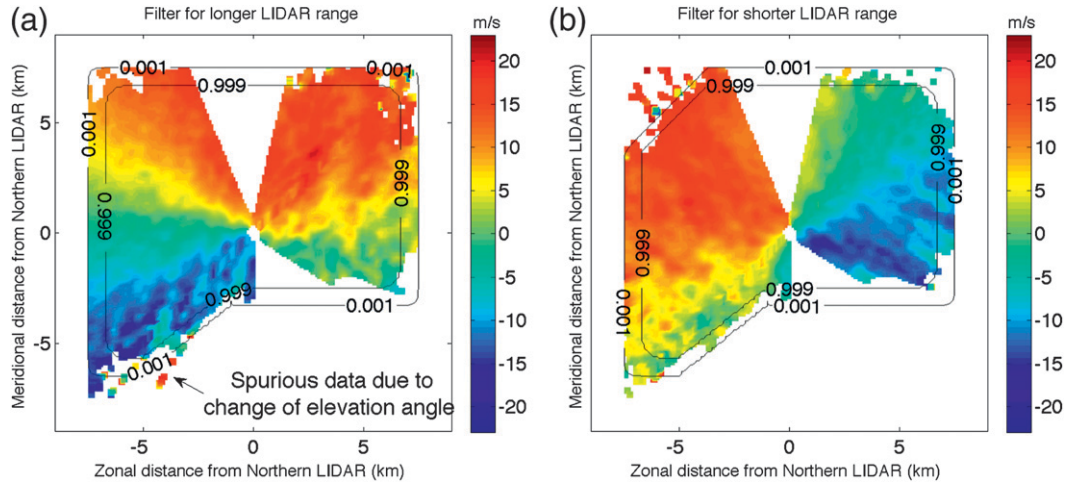


FIG. 2. Lidar outputs on two different days and filter functions. Spurious data due to the terrain are identified by the arrow in (a). They are responsible for artificial structures and are excluded in trajectory integration. (a) 1426 UTC 19 Apr 2008; the filter uses full data at the top-left corner. (b) 0658 UTC 6 Aug 2008. Spurious data due to rain are removed by the corresponding filter.

Once we have this global flow, in the second step, we can integrate fluid trajectories from the velocity field and compute the finite-time Lyapunov exponents based on the global flow:

$$\sigma(t; t_0, \mathbf{x}_0) = \frac{1}{2|t - t_0|} \times \ln \left\langle \lambda_{\max} \left\{ \left[ \frac{\partial \mathbf{x}(t; t_0, \mathbf{x}_0)}{\partial \mathbf{x}_0} \right]^T \frac{\partial \mathbf{x}(t; t_0, \mathbf{x}_0)}{\partial \mathbf{x}_0} \right\} \right\rangle. \quad (5)$$

Preservation of the ridges in the extended velocity field will be ensured by the linearity of  $\mathbf{v}$  in the spatial variables  $\mathbf{x}$  outside the grid  $\mathcal{G}$ . The FTLE field associated with a linear vector field is constant, with its value converging to the largest Lyapunov exponent of the origin of the homogeneous part of the vector field.

Generally,  $\Delta$  measures the size of a small transition region around the grid boundary in which the original velocity field  $\mathbf{u}$  is modified. This motivates the choice of a small  $\Delta > 0$ . At the same time, if the original velocity field  $\mathbf{u}$  is strongly nonlinear then selecting  $\Delta$  that is too small will create large gradients for Eq. (5) in the transition region, resulting in potential numerical difficulties. Therefore, the optimal choice of  $\Delta$  depends on the application considered.

#### 4. LCS over Hong Kong International Airport

We now use the FDFTLE method described above to locate LCS in wind velocity data from coherent Doppler radar and lidar observations over Hong Kong International Airport. For such observational datasets, two constraints

limit the straightforward extraction of LCS using the FTLE field Eq. (5). First, remote sensing only recovers the line-of-sight velocity component relative to the instrument, and hence the cross-beam components of the velocity field are not directly available. Second, lidar observations have a limited range of detection outside of which the wind velocity remains unknown; this leads to edge effects and noise in LCS detection as described in the introduction.

We address the line-of-sight constraint by employing variational wind retrieval techniques, while we handle the limited-domain problem using the FDFTLE technique described in the previous section.

Figure 2 illustrates the lidar outputs and filters used on two different days. For both panels, the inner isocontours mark the edges of the subset  $\mathcal{G}^0$  and the outer isocontours are the boundaries where flow becomes  $\mathbf{v}_L$ . The transition region is in between the two isocontours. The filter is adjusted to specific datasets when the lidar range varies. As seen in Fig. 2a, there are spurious data at the lower-left corner of the domain due to small changes in the scanning angles. These spurious data are persistent in most observations because they are obtained next to a mountain gap; small changes in the scanning angle between different PPI scans always result in such intermittency. Their presence creates artificial structures that contaminate the LCS. They are removed by taking a nonrectangular shape, as illustrated in Fig. 2a. This filter also removes the unreliable data inside the unresolved regions south of HKIA. In addition, on a day of slightly limited lidar range, we find that there are spurious data near the top-left corner of the wind retrieval domain. These spurious

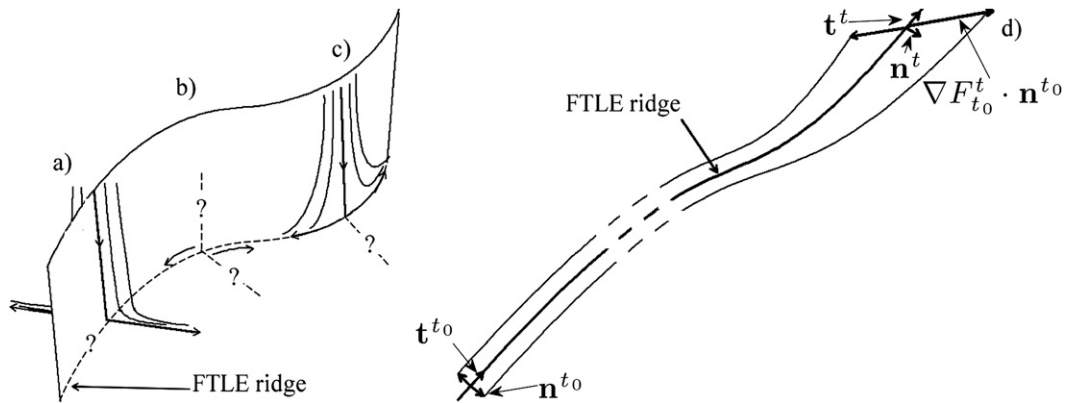


FIG. 3. Motion relative to a forward-time FDFTLE ridge. Point a shows stretching transversal to the structures. Downdraft is illustrated along the transversal stretching but it is not a necessary condition for stretching to exist. Point b shows shear parallel to the structure. Transversal and parallel strains can take any sign if the shear is large enough. Point c shows straining parallel to the structures. It must be associated with large transversal stretching or with parallel shear. Point d shows vectors used to quantify shear and strains relative to LCS.

data are removed by a further modification of the filter as illustrated in Fig. 2b.

With the extrapolation scheme, trajectories near the end of the domain are allowed to fully separate after exiting the boundaries. Since the external flow is linear, no extra nonlinearity is introduced from this scheme and hence no extra highlighters (ridges) will appear in the FTLE field, whereas all the nonlinearity inside the domain will be accounted for. As a comparison, if we stop trajectories at the boundaries, nearby trajectories, even under strong stretching, will only separate mildly if they started near the downwind boundaries; so they may fail to become highlighters because of the artificial no-slip boundary condition.

Since we are analyzing a two-dimensional slice of a three-dimensional flow, stretching and folding highlighted in the FTLE field could come from several different possible sources. For example, repelling LCS could arise from the stretching of trajectories in the conical surface or supply of trajectories from across this surface. The lidar conical scans at HKIA have small elevation angles, hence at least close to the lidars, the conical surface is very close to the ground. With this consideration, stretching confined in the conical surface corresponds to diverging horizontal wind shear, and stretching involving motion across the conical surface corresponds to downdrafts. Likewise, attracting LCS correspond to converging wind shear and updrafts near the lidars.

We use another quantity derived from Lagrangian trajectories to differentiate the sources of stretching and folding as well as horizontal wind shear highlighted in the FTLE fields. Assuming that the three-dimensional atmospheric flow is divergence-free, one can integrate the instantaneous horizontal divergence along a trajectory  $\mathbf{x}(t; \mathbf{x}_0, t_0)$  and take its average over time,

$$\text{DIV}_{t_0}^t(\mathbf{x}_0) = \frac{1}{|t - t_0|} \int_{t_0}^t \left[ \frac{\partial u(\mathbf{x})}{\partial x} + \frac{\partial v(\mathbf{x})}{\partial y} \right] dt, \quad (6)$$

which we refer to as the Lagrangian divergence.

If the airflow is purely two-dimensional along the conical surface, Lagrangian divergence will be zero yet we still see maximizers of the FTLE fields. They correspond to stretching and folding of fluid particle trajectories on the conical surface. On the other hand, if there is consistent cross-surface motion, Lagrangian divergence will be nonzero. The absolute sign in front of the integral on the right-hand side of Eq. (6) ensures that DIV maxima correspond to persistent downdrafts when trajectories are integrated in forward time and persistent updrafts when trajectories are integrated in backward time. As such, locally the strongest updrafts and downdrafts should be identified as FTLE maxima together with DIV maxima, yet horizontal wind shear is identified as FTLE maxima that do not have such correlations. In our datasets, it is found that Lagrangian divergence starts to differ significantly from Eulerian divergence when the integration time is over 90 s. The major structures emerge when integration time exceeds 3 min.

Relative horizontal motion near FTLE highlighters (ridges) can be identified as stretching (folding) perpendicular to the structures ( $\text{STR}_{\perp}$ ), along the structures ( $\text{STR}_{\parallel}$ ), or shear (SHR) along the structures. The real flow structure usually appears as the combination of the three.

Take the forward-time FTLE ridge as an example. Trajectory separation could be transversal to the ridge, as illustrated in Fig. 3a. In this case, trajectories must be supplied either vertically or horizontally. If the supply is from vertical motion (measured by DIV), it must appear

as a downdraft. Strain along the structures can take either sign to conserve volume. If the supply is from horizontal motion, then parallel strain must be negative, and the vertical motion can appear as a downdraft or updraft. Since strong contraction is transversal to stretching under this situation, the ridges in backward-time FTLE should be transversal to the ridges in forward-time FTLE. This does not appear to be the predominant character of the FTLE ridges that we observe from the HKIA data, so transversal stretching can be associated with downdrafts.

Another mechanism for large trajectory separation is horizontal shear, as illustrated in Fig. 3b. In this case, vectors perpendicular to the LCS are separated in the direction tangential to the structures. The vertical and horizontal motions are secondary and can take any sign. The final measure of separation of trajectories is the parallel strain, illustrated in Fig. 3c. Note that parallel strain alone does not give rise to FTLE ridges in the observed directions; it must be associated with transversal stretching or horizontal shear. Without them, the direction of the largest amount of separation would appear to be along the structures and hence the ridges would be transversal to the direction of the strain. Therefore, parallel strain measures a tendency of deformation relatively smaller than the other three measures (DIV, STR<sub>⊥</sub>, and SHR). We nevertheless include this measure to provide a complete picture of the flow structures.

Figure 3d illustrates the various vectors used to derive Lagrangian versions of STR<sub>⊥</sub>, STR<sub>∥</sub>, and SHR. Specifically, we define an eigenvector normal to a ridge at time  $t$  as  $\mathbf{n}^t$  and an eigenvector tangent to a ridge at time  $t$  as  $\mathbf{t}^t$ . As described in Shadden et al. (2005) and Mathur et al. (2007), points on two-dimensional FTLE ridges satisfy the requirements that the smallest eigenvalue of the Hessian matrix must be negative and its eigenvector perpendicular to the gradient vector of the FTLE field. The other eigenvector is tangent to the FTLE ridges. We densely seed initial conditions in the domain so that there are trajectories very close to the ridges. This ensures that there will be enough trajectories near the ridges at the end of integration, because the ridges are repelling in nature. The eigenvectors associated with the Hessian matrices of the FTLE field are extracted at the beginning and the end along a trajectory. For initial conditions near the ridges, the quantities

$$\begin{aligned} \text{STR}_{\perp} &= \frac{1}{|t - t_0|} \ln[(\mathbf{n}^t)^T \cdot \nabla \mathbf{F}_{t_0}^t \cdot \mathbf{n}^{t_0}], \\ \text{STR}_{\parallel} &= \frac{1}{|t - t_0|} \ln[(\mathbf{t}^t)^T \cdot \nabla \mathbf{F}_{t_0}^t \cdot \mathbf{t}^{t_0}], \quad \text{and} \\ \text{STR} &= \frac{1}{|t - t_0|} \ln[(\mathbf{t}^t)^T \cdot \nabla \mathbf{F}_{t_0}^t \cdot \mathbf{n}^{t_0}] \end{aligned} \quad (7)$$

measure the average stretching and shear relative to the LCS. Note that the first two measures agree with the normal and tangential Lyapunov-type numbers defined by Fenichel for general invariant manifolds (Fenichel 1972).

It is important to appreciate that the FDFTLE at time  $t$  in this calculation is not based on trajectory integration starting from  $t$ . Indeed, by our choice of integration time, trajectories enter a different state at the end of integration so FDFTLE highlighters reveal different material lines as repellers. To evaluate trajectory behaviors between  $t_0$  and  $t$ , the same FDFTLE field is used, yet advected with the flow. This ensures that the same material lines on the ridges are evaluated throughout the integration time (we are evaluating Lagrangian motion relative to these material lines). Within this framework, the Hessian matrix of the FTLE field at time  $t$  is approximated by densely populating initial conditions at time  $t_0$  and advecting the scalar field with the trajectories, then interpolating onto regular grids and evaluating  $H_t$ . To our best knowledge, apart from the linear extrapolation scheme that allows trajectory integration outside an open domain, the Lagrangian versions of horizontal motions are also new. Previously, an instantaneous version of STR<sub>⊥</sub> was used in Mathur et al. (2007), which does not necessarily reveal the true Lagrangian motion since it is an Eulerian quantity. The measures developed here also differentiate shear from parallel strain, both of which were previously considered shear.

Armed with the four measures (DIV, STR<sub>⊥</sub>, STR<sub>∥</sub>, and SHR), we can infer the overall airflow motion following a Lagrangian observer. The accuracy of these criteria is tested by comparison with vertical RHI scans, which are not used in the horizontal wind retrieval.

### 5. LCS based on retrievals

We analyze the lidar data under three different weather conditions between April 2008 and February 2009. These days are chosen because of the strong wind speeds observed, which may lead to interesting turbulent coherent structures. There are two lidar systems installed at HKIA; all cases are analyzed based on data from the northern lidar, as it takes PPI scans at smaller elevation angles more suitable for airplane approaches. We only work with a single lidar retrieval, as wind retrieval from two lidars at HKIA is still under development at HKO.

Before the analyses of different cases, we first integrate fluid particle trajectories to obtain the time series of instantaneous divergence and identify the time scale of coherent turbulent motions. The result indicates that an appropriate time of integration is around 5 min, in line with the turbulence characteristics at HKIA observed in Chan and Shun (2005). As a result, the LCS we extract

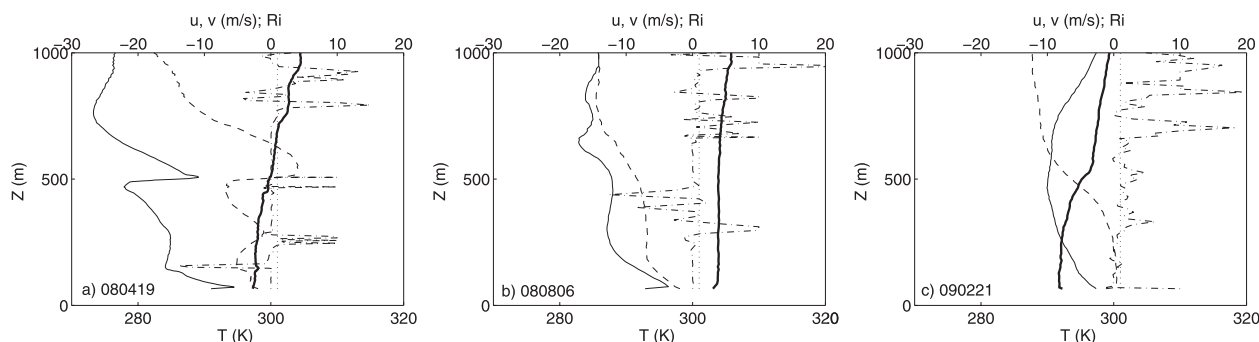


FIG. 4. Quantities derived from balloon measurements on (a) 19 Apr 2008, (b) 6 Aug 2008, and (c) 21 Feb 2009. In (a)–(c), the thick solid curves denote the potential temperature (axes at the bottom), the thin solid curves show the zonal wind, the thin dashed curves show the meridional wind, the dashed–dotted curves denote the gradient Richardson number  $Ri$ , and the thin vertical lines reference  $Ri = 1$ , indicating regions of absolute stability to its right (axes at the top).

contain three frames of lidar data and reveal structures that are persistent over the integration time.

To contrast the three synoptic conditions (a springtime tropical cyclone in April 2008, a summer cyclone in August 2008, and a spring easterly in February 2009), we plot quantities derived from balloon measurements at the King’s Park Meteorological Station near HKIA. Figure 4 reveals such information at King’s Park; the thick curves indicate the potential temperature, and the thin solid (dashed) curves are the zonal (meridional) winds. Based on these data we can derive the gradient Richardson number  $Ri$ , which is plotted in dashed–dotted curves. The thin vertical lines are reference lines of  $Ri = 1$ . To the right of this line, the fluid layer has absolute stability; to the left of this line, the fluid layer is subject to shear or convective instabilities. Note that the axis for the last four curves is on the top of Figs. 4a–c. As seen, the boundary layer is least stratified in Fig. 4b (summer cyclone), yet the vertical shear at the base of the boundary layer in both 2008 cases is stronger than the spring easterly case in 2009. These differences could be the reason leading to the different scales of structures observed from the following LCS analyses. It is unclear if the different prevailing wind directions may be related to the onset and location of horseshoe–counterrotating vortices. More cases would be needed to establish this relationship, if any.

On 19 April 2008, a tropical cyclone made landfall over the western coast of southern China and moved inland on a northeastern track. Rainbands and strong southerly winds associated with the tropical cyclone affected Hong Kong. After the rainbands, there was good data coverage from 1330 to 2000 UTC, giving us a reasonable window to analyze the flow structures associated with the southerly flow. Direct output from the lidar and wind retrieval at 1429 UTC is seen in Fig. 1. The results are interpreted first on an individual basis, then on overall flow conditions.

Figure 5 epitomizes the Lagrangian analyses for individual structures. In Fig. 5a, forward-time FTLE maxima can be identified at 1429 UTC (the lower left corner). The material lines on the ridges are extracted using the method described in Mathur et al. (2007), and shown as a collection of black dots. We initialize a few trajectories near the strongest ridge to study their motion relative to the structure. The trajectories (in cyan) are shown for 5 min, and particle locations are marked at 2.5-min intervals as magenta dots. The three patches of color maps show the evolution of the forward-time FTLE field, as advected by the flow, with the time labeled next to them. Clearly, the FTLE maxima act both as repellers, such that nearby trajectories are pushed away from the structure, as well as wind shear, since trajectories also appear to slide along the structure. These motions are quantified with the horizontal measures  $STR_{\perp}$ ,  $STR_{\parallel}$ , and  $SHR$ , evaluated at 1429 UTC, and shown next to the trajectory plot. Figure 5a shows  $STR_{\perp}$ ; the measure being predominantly positive (in red) near the LCS indicates a repelling motion of the ridges. Figure 5b shows  $STR_{\parallel}$ . It is found that parallel strain is not too strong, except at the bottom of the map. Figure 5c shows  $SHR$ . Clearly shear is strong near the ridges, in agreement with the behavior of the trajectories. In the inset of Fig. 5a, we show the 90th percentile of  $DIV$  as an isocontour in white. This indicates regions of strong downdraft. From this information we estimate the flow structure associated with these FTLE maxima as the schematics shown in the lower right corner of Fig. 5a. This schematic plot is understood as the flow structure an observer would see following the motion of a Lagrangian particle and the trajectories are all relative to the observer. In this Lagrangian view, the core of the downdraft is marked by the FTLE maxima. Nearby trajectories also appear to be sinking but not as significant as those directly above the LCS. They are repelled away as well as stretched to the side as they descend. Figure 5b shows

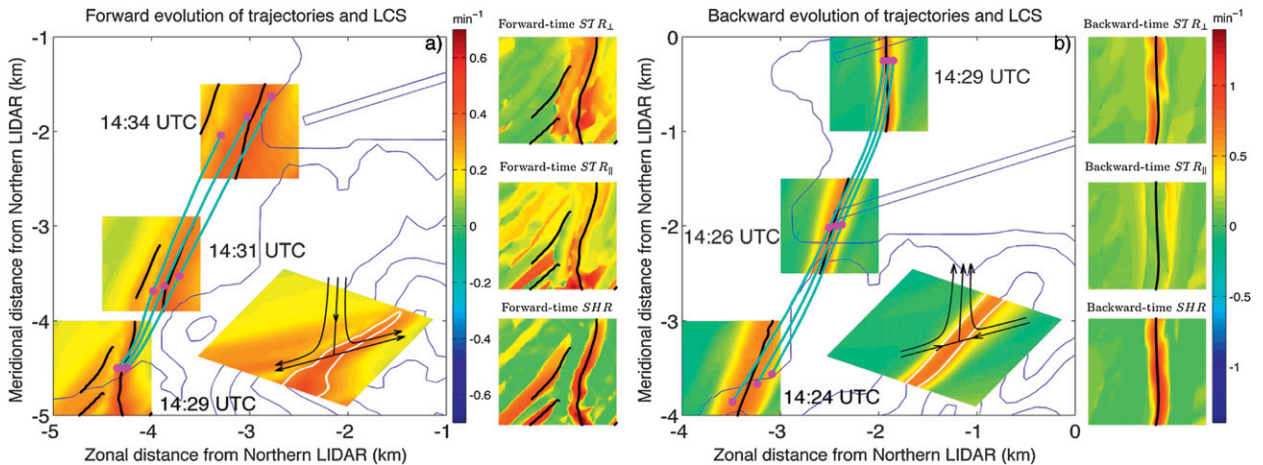


FIG. 5. Relative motion of trajectories near LCS and horizontal measures for 19 Apr 2008. (a) Trajectories near a forward-time FDFTLE ridge. (b) Trajectories near a backward-time FDFTLE ridge. Blue isocontours show terrain at 100-m intervals. The runway strips are also shown as rectangles. The cyan curves show the evolution of three different fluid trajectories near an FDFTLE ridge over 5 min. Magenta dots mark the location of these fluid particles at 2.5-min intervals. The color maps beneath the magenta dots are FDFTLE fields near the fluid particles extracted at 2.5-min intervals. Ridges of FDFTLE are extracted and shown as the collection of black dots. Time is labeled next to these color maps. The insets at the lower-right corner of (a) and (b) show schematics of the inferred flow structures associated with the LCS, along with the 90th percentile of DIV fields, indicating strong vertical motion. To the right of the (a) and (b) are (from top to bottom) the three color maps of  $STR_{\perp}$ ,  $STR_{\parallel}$ , and  $SHR$ , respectively. Ridges are also shown for comparison with the horizontal measures.

similar analyses for an attracting structure extracted at 1429 UTC. The only difference is that trajectories are traced in backward time to evaluate the behavior around the FTLE maxima. Schematics of flow structures relative to a Lagrangian observer and the horizontal measures are also shown. In both panels, the nearby terrain is shown with blue isocontours and the blue rectangles indicate the location of the airstrips, thus the LCS relative to the runways can be directly seen.

Figure 6 summarizes the results from Lagrangian analyses at this time (1429 UTC). Computed from the retrieved wind velocity at a PPI angle of  $1.4^{\circ}$ , the color plot in Fig. 6a shows the forward-time FTLE and that in Fig. 6b shows the backward-time FTLE. Superimposed on these color maps are the isocontours of DIV at the 90th percentile; the respective values are noted in the figure caption. The small regions inside the isocontours indicate regions of strong transversal motion across the conical surface over the integration time. The units of the color maps in Fig. 6 are  $\text{min}^{-1}$ . The two blue square boxes are the locations of the individual LCS discussed in Fig. 5.

When visually inspecting the FTLE fields and DIV contours, we find that there is a good correlation between the two. This indicates that most of the LCS we extract correspond to structures that carry vertical motions. The uncorrelated structures have to correspond to strong horizontal wind shear since that is the only possible way leading to strong trajectory separation.

The structures are best understood from Fig. 6b. Several hairpin-shaped structures are found to the southwest

of the airport, traversing the runway corridors. We label the two structures just above the airport as A and B. To understand their origin we trace these LCS backward in time and find that A arises because of the patch of the LOS velocity anomaly marked by the white ellipse on the lhs of Fig. 1a, whereas B is associated with the anomaly highlighted by the other ellipse on the rhs. These regions are highlighted by the two crosses in Fig. 6b. From the streamlines in Fig. 1b, airflow enters from the southwest and follows the coastline of Lantau Island. The two patches of anomalies appear as regions of slower LOS velocity compared to the background flow and are attached to the lee of two mountains. Their existence could be due to fast gap flow taking over the slower flow over mountains. As trajectories move through the patches, strong contraction is experienced at the leading edge. This contraction effectively created structures A and B. The two prongs of the hairpins mark sets of fluid particles that attracted nearby trajectories the most through the existence of the anomalies, and they get advected downstream by the background flow as well. On the rhs of Fig. 6b, several attractors appearing as streaks are present in the domain (labeled C). These streaks can roughly be identified from the LOS velocity maps in Fig. 1 as streaky anomalies. However, LCS reveal them with high clarity.

Figure 6a shows the FTLE and DIV fields computed in forward time. We note that there are two major red patches in Fig. 6a correlated with the two crosses, marking the generation sites of hairpins A and B. These red patches are also caused by the two disturbances. Trajectories

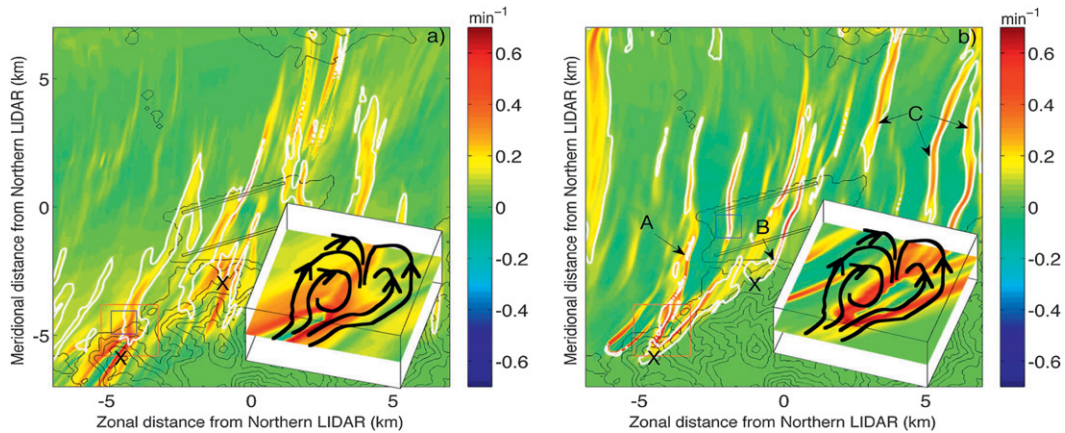


FIG. 6. The LCS obtained from the 2D wind retrieval at 1429 UTC 19 Apr 2008. (a) Forward-time FDFTL field. Maximizers indicate repelling structures. The isocontours correspond to DIV with a value of 0.0015. (b) Backward-time FDFTL field. Maximizers indicate attracting structures. The isocontours correspond to DIV with a value of 0.001. Black boxes contain structures discussed in Fig. 5; the red boxes contain a horseshoe vortex. Schematics of this horseshoe vortex are shown as insets.

experience stretching as they flow through the trailing edges where the disturbances pick up speed to match the background flow. It is interesting to note that although the red patches in Fig. 6a also look like hairpins, the prongs do not correlate with DIV. Furthermore, patches of DIV maxima are immediately downwind of the generation sites marked by the crosses. Combining this with Fig. 6b, the structures at the head of the hairpins may be recirculating bubbles attached to the mountains. The prongs are due to horizontal wind shear created by flow blockage from the recirculating bubbles. The background flow carries the edge of this bubble downstream, resulting in the two prongs of updraft seen in Fig. 6b and in between them a downdraft where trajectories return to the conical surface. This indicates that the hairpins may be a two-dimensional slice of horseshoe vortices near ground. The schematics of the horseshoe structure inferred from the hairpins inside the red boxes (same structure) are plotted at the lower right corners. To the east of the airport, similar to Fig. 6b, several repelling streaks are present. Based on the above observations, we conclude that at this moment the major flow structures at HKIA are a couple of generation sites for horseshoe vortex structures to the west of the airport, with hairpin structures traversing the runways. To the east of the airport, several alternating repelling and attracting streaks are generated, probably due to the mountain gaps, and they transect the runway corridors.

On 6 August 2008, a tropical cyclone moved north-eastward over the northern part of the South China Sea. It brought about strong easterly winds in Hong Kong. A scattered rain shower was persistent, which left quality data few and far between. Additionally, raindrops attenuated the laser beams, which resulted in a shorter

detection range of the lidars. As a result, we use the modified filter shown in Fig. 2b for the FDFTL extraction. For those few groups of consecutive data, we extract LCS and decipher the flow condition. One window was between 0641 and 0707 UTC. Structures were extracted at 0658 UTC so there is room for both forward- and backward-time integration.

Figure 7 shows the overall LCS in the domain. There appear to be a lot more streaky structures originating from Lantau Island than for the spring tropical cyclone case. The basic flow structure is alternating attractors and repellers along the coastlines. These streaks do not seem to extend as far as those shown in Fig. 6 and they lose coherence not far from the runways. Trajectory analyses and horizontal measures indicate that, unlike the spring tropical cyclone case, there is not much horizontal shear associated with the structures; trajectories are repelled/attracted transversal to the structures. The schematic view of the flow structures inside the small square box is illustrated at the upper left corners. There seems to be a counterrotating vortex in this region as depicted from the schematics and we do not notice hairpin structures associated with this episode of synoptic flow.

On 21 February 2009, a ridge of high pressure over the southeastern coast of China brought strong easterly winds to Hong Kong in a relatively stable boundary layer. The lidar range is slightly affected by rain, thus we still use the filter in Fig. 2b. Figure 8 shows LCS extracted at 0359 UTC. At this time, a couple of hairpin structures are found to be attached to the mountains east of the airport, marked by crosses (one of them is actually outside the plotted domain). There appear to be much fewer flow streaks as compared to the summer tropical cyclone.

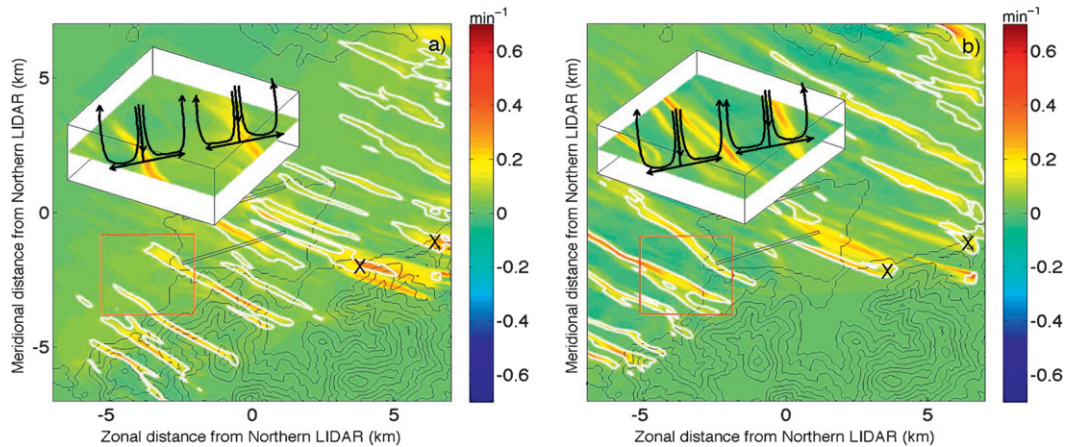


FIG. 7. The LCS obtained at 0658 UTC 6 Aug 2008. (a) Forward-time FDFLE field. Maximizers indicate repelling structures. The isocontours correspond to DIV with a value of 0.0013. (b) Backward-time FDFLE field. Maximizers indicate attracting structures. The isocontours correspond to DIV with a value of 0.001. The red boxes contain several counterrotating vortices. Schematics of these vortices are shown as insets.

However, the streaks and the flow structures appear to be larger in scale and longer in downstream distance. Horizontal measures show that these streaks again do not carry much horizontal shear motion along the structures; they seem to be larger-scale counterrotating vortices. The weaker and less gusty winds as well as the stable boundary layer in this case may contribute toward the formation of vortices of a larger extent as compared to the episode of the summer easterly (see Fig. 4). The schematics of flow in the red squares are also shown in the insets.

Aside from the PPI scans, the lidars at HKIA perform RHI scans every 30 min or so. The three cases presented here all correspond to the time of an RHI scan at 258° azimuth, along the runway corridor. We compare LCS

with RHI scans to confirm the structures we deduce from the data. RHI scans are also performed at 163° azimuth, pointing into a mountain gap. We ignore this scan as this azimuthal angle is subject to sector blanking in the PPI scans, so structures extracted along this direction may not be correct. Also the RHI scan is performed at higher elevation angles (3.6° and up), making direct comparison difficult.

We only illustrate the comparison with RHI scan at 1429 UTC 19 April 2008, as the other comparisons follow the same reasoning and show similar results. The results are shown in Fig. 9. Note that in general Lagrangian and Eulerian quantities should not be compared directly, as they reveal different things. In this study our integration time is only 5 min; accordingly LCS contains three frames

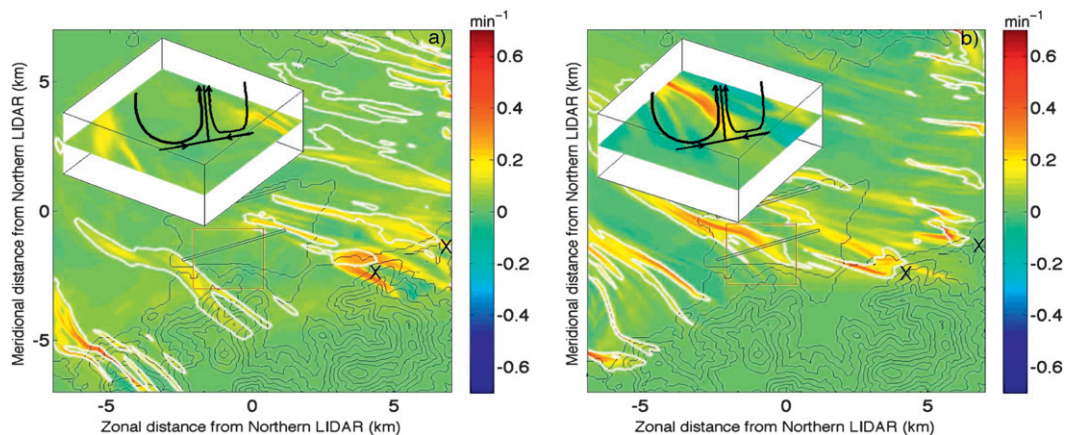


FIG. 8. The LCS obtained at 0359 UTC 21 Feb 2009. (a) Forward-time FDFLE field. The isocontours correspond to DIV with a value of 0.0012. (b) Backward-time FDFLE field. The isocontours correspond to DIV with a value of 0.001. The red boxes correspond to the location of the counterrotating vortices drawn in the insets.

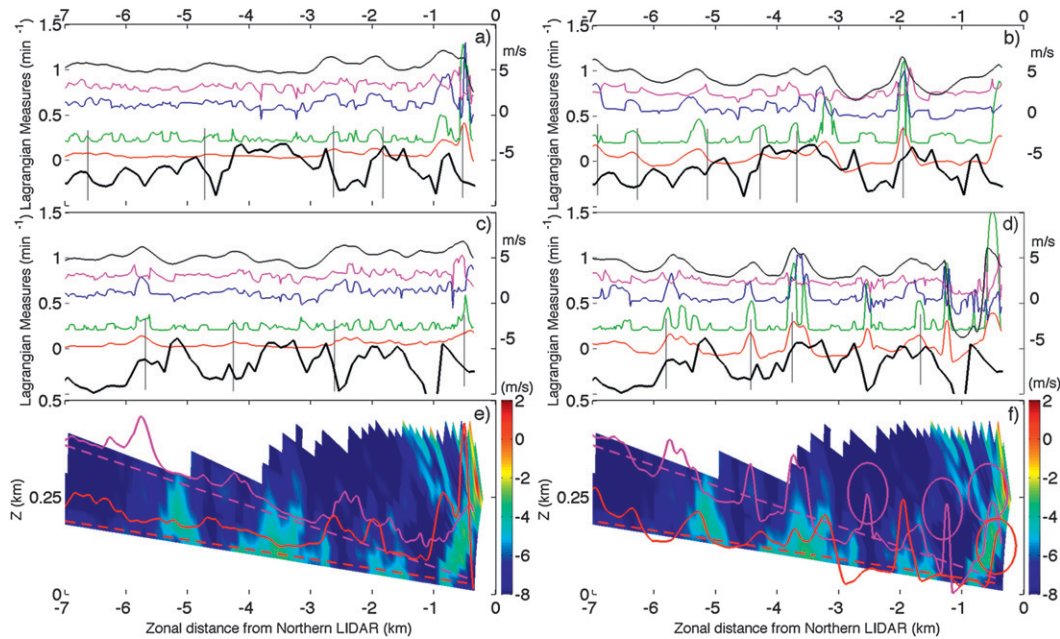


FIG. 9. Comparison between LCS and RHI scan at 1429 UTC 19 Apr 2008. (a) Comparison of various quantities along  $258^\circ$  azimuth, at elevation angle  $1.4^\circ$ . The lines with different colors correspond to the following: thick black—LOS velocity from the RHI scan, red—forward-time FTLE, green—SHR, blue— $STR_{\perp}$ , magenta— $STR_{\parallel}$ , and black—DIV. (b) As in (a) but the Lagrangian measures are from backward-time trajectory integration. Note that SHR,  $STR_{\perp}$ ,  $STR_{\parallel}$ , and DIV have been shifted upward for clarity of the plots. (c) As in (a) but for elevation angle  $3.0^\circ$ . (d) As in (b) but for elevation angle  $3.0^\circ$ . RHI scan superimposed with (e) forward-time and (f) backward-time FTLE at  $1.4^\circ$  and  $3.0^\circ$ . Color shades represent the LOS velocity. The four circles denote FTLE ridges corresponding to horizontal shear.

of data. This makes direct comparison somewhat meaningful. Figure 9a shows the comparison between forward-time Lagrangian measures and the LOS velocity. The LOS velocity obtained during the RHI scan is shown in thick black, with its axis on the right. The red curve in Fig. 9a shows the forward-time FTLE from the  $1.4^\circ$  scan. A couple of major peaks can be identified near the lidar, and a few smaller peaks are found between 3 and 2 km from the lidar. The black curve showing DIV indicates that downdrafts are associated with these peaks. The magenta curve showing  $STR_{\parallel}$  indicates that there is not much stretching tangential to the structures (into the paper). The blue curve showing  $STR_{\perp}$  indicates that there is repelling motion transversal to the structures. In the context of LOS velocity, the above behaviors correspond to an increase of velocity toward the lidar as one approaches the lidar, which is exactly the behavior of the LOS velocity shown in the figure. (The LOS velocity is turning more negative, and thus increasing toward the lidar.) These curves are shifted by 0.2 intervals so direct comparison of the structures is more apparent. Their axes are on the lhs of the panel. Similar curves for the  $3.0^\circ$  scan are also shown in Fig. 9c. In Fig. 9e, the RHI scan at different elevation angles is superimposed with the forward-time FTLE derived from the

$1.4^\circ$  and  $3.0^\circ$  PPI scans, shown in red and black, respectively. As we can see, the LOS velocity pattern in the RHI scan shows four patches of slower velocity embedded in a background of faster velocity toward the lidar. Peaks of forward-time FTLE are then expected to be at the trailing edges of these patches, as trajectories separate at these locations. The peaks of FTLE in Fig. 9e in general appear to agree with the expectations. This correspondence is also revealed in Figs. 9a,c, with peaks of FTLE in general correlated to negative slopes of LOS velocity. The specific FTLE peaks and LOS velocity slopes where this correspondence may be drawn are connected by the black vertical lines.

Figures 9b,d,f show the same analyses for backward-time trajectories. In this case, peaks are expected to correlate with the leading edge of the patches as trajectories approach each other at these locations and turn into updrafts. We again see a correspondence between the backward-time FTLE peaks and the leading edges of the patches. Similar to Figs. 9a,c, we connect peaks of FTLE with positive slopes of LOS velocity in Figs. 9b,d. For backward-time analyses, we find that there are a few exceptions where FTLE peaks do not correspond to leading edges of LOS velocity. The horizontal measures shown as the green curves in Figs. 9b,d indicate that

these peaks are associated with strong horizontal shear yet relatively weak Lagrangian divergence. Thus the peaks correspond more to wind shear.

Since PPI and RHI scans cannot be performed at the same time, even a direct comparison between the LOS velocity based on a true RHI scan and on interpolated PPI scans yields differences. With this consideration in mind, the correspondence between LCS and the RHI scans is reasonable, hence confirming the flow structures inferred by combining the FTLE, DIV, STR<sub>⊥</sub>, STR<sub>∥</sub>, and SHR fields.

## 6. Conclusions

We have used a recently developed algorithm, the FDFTLE method, to extract Lagrangian coherent structures from two-dimensional wind data retrieved from lidar measurements. By extrapolating the retrieved wind into a linear global flow, we have extended Lagrangian trajectory integration beyond the observational domain such that nonlinearity of the flow in the interior is unaffected. Integration time is chosen by an examination of the time series of the horizontal divergence such that trajectories do not lose coherence over this time scale. To infer the three-dimensional flow structure, we have employed criteria to differentiate between updrafts, downdrafts, horizontal stretching, and horizontal wind shear associated with the LCS.

For the different cases analyzed, we have revealed several types of organizing structures subject to the synoptic flow conditions. Based on the two-dimensional LCS and trajectory behaviors, we infer that horseshoe vortex structures and counterrotating vortices are prevalent in these cases. When present, the horseshoe vortices are found to attach to the lee of mountain peaks, as patches of recirculating bubbles with arms of counterrotating vortices. The alternating attractors and repellers indicate counterrotating vortices that could be part of a horseshoe vortex generated outside of the lidar observable domain. They are usually associated with gap flows. In addition to these transversal structures, horizontal wind shear is found to sometimes accompany the LCS. The length scales of these structures vary with the synoptic flows. Further comparisons show good correlation between the LCS with vertical structures inferred from the RHI scans. Note that since RHI scans are only available at a few azimuthal angles, the LCS provides a complete picture of the near-ground vertical and horizontal structure of the flow.

Since the LCS are extracted from FDFTLE (which characterizes the separation of nearby trajectories), the LCS we identify are not affected by choices of frame. Such a frame-independent structure characterization is important, as airplanes are moving observers that are not

attached to the ground. An Eulerian description of the flow observed from the ground will be different from that observed on a plane, which makes flow diagnosis arbitrary between weather forecasters and pilots. The flow structures, on the other hand, should not be arbitrary as the relative separation of trajectories is frame independent. It is this very motion that creates headwind changes for airplanes, which are the hazards we want to identify.

Additionally, LCS reveal important structures with high clarity. This is apparent from comparing any of Figs. 6, 7, 8 with LOS velocity and streamlines in Fig. 1. With this strong contrast, one can accurately identify important flow structures near the airport. Because the TDWR data discussed in Shun et al. (2003) also return the LOS velocity as outputs, it will be interesting to perform wind retrieval and LCS extraction for that dataset to find and compare characteristic flow structures in rainy weather.

For the operational use of LCS as a tool to identify turbulent flow structures in real time, a limitation arises from the nature of Lagrangian analysis. In particular, we need to integrate trajectories over time and forward-time analyses are not possible, as flow data at later times are not yet available. This leaves downdrafts and repelling structures unrevealed (shear-type structures can still be extracted from backward-time integration). Computing forward-time FTLE at an earlier time and then advecting this scalar field with the flow is not implementable as the structures really only reveal behavior during the integration time, and it is irrelevant with LCS at the later time.

We also note that the wind retrieval technique used here is based on the assumption that a few modes of polynomial expansion will capture major features of the flow. This leaves some uncertainty in the velocity component transversal to the lidar beams, as no physics is implied by the polynomial expansion of a flow. Moreover, since we are limited by the length of the PPI scan intervals, variation of flow structures is only captured by three frames. For more accurate structure extraction to capture the evolution of LCS, better temporal resolution is desired.

Additional steps are under consideration to address the above difficulties. One promising approach is to use submesoscale simulation initiated from lidar measurements to constantly forecast the velocity field 5 min ahead, and use the forecast data to integrate trajectories into the future. This approach not only allows analyses of forward-time trajectories, but also enables three-dimensional structure extraction for better view of the flow near the airport. Doing a 5-min forecast may not be too computationally costly either.

In Part II, we examine airplane approaches during the cases studied to understand the correlation between LCS and jitters that airplanes experienced. This is expected to lead to a better understanding of the causes of missed

approaches and thus improve warnings for airflow hazards near airports.

*Acknowledgments.* We acknowledge three anonymous reviewers for their thorough reading and helpful comments that improved the manuscript. WT also acknowledges the support from NSF Grant ATM-0934592.

#### REFERENCES

- Chan, P. W., and C. M. Shun, 2005: Numerical simulation of vortex shedding observed at the Hong Kong International Airport using a shallow water model. *Croat. Meteor. J.*, **40**, 27–30.
- , and A. M. Shao, 2007: Depiction of complex airflow near Hong Kong International Airport using a Doppler LIDAR with a two-dimensional wind retrieval technique. *Meteor. Z.*, **16**, 491–504.
- Coulliette, C., F. Lekien, J. D. Paduano, G. Haller, and J. E. Marsden, 2007: Optimal pollution mitigation in Monterey Bay based on coastal radar data and nonlinear dynamics. *Environ. Sci. Technol.*, **41**, 6562–6572.
- Fenichel, N., 1972: Persistence and smoothness of invariant manifolds for flows. *Indiana Univ. Math. J.*, **21**, 193–226.
- Haller, G., 2001: Distinguished material surfaces and coherent structures in three-dimensional fluid flows. *Physica D*, **149**, 248–277.
- , 2005: An objective definition of a vortex. *J. Fluid Mech.*, **525**, 1–26.
- Jeong, J., and F. Hussain, 1995: On the identification of a vortex. *J. Fluid Mech.*, **285**, 69–94.
- Lekien, F., C. Coulliette, A. J. Mariano, E. H. Ryan, L. K. Shay, G. Haller, and J. E. Marsden, 2005: Pollution release tied to invariant manifolds: A case study for the coast of Florida. *Physica D*, **210**, 1–20.
- Mathur, M., G. Haller, T. Peacock, J. E. Ruppert-Felsot, and H. L. Swinney, 2007: Uncovering the Lagrangian skeleton of turbulence. *Phys. Rev. Lett.*, **98**, doi:10.1103/PhysRevLett.98.144502.
- Qiu, C. J., and Q. Xu, 1992: A simple adjoint method of wind analysis for single-Doppler data. *J. Atmos. Oceanic Technol.*, **9**, 588–598.
- , A. M. Shao, S. Liu, and Q. Xu, 2006: A two-step variational method for three-dimensional wind retrieval from single Doppler radar. *Meteor. Atmos. Phys.*, **91**, 1–8.
- Shadden, S. C., F. Lekien, and J. E. Marsden, 2005: Definition and properties of Lagrangian coherent structures from finite-time Lyapunov exponents in two-dimensional aperiodic flows. *Physica D*, **212**, 271–304.
- Shun, C. M., and P. W. Chan, 2008: Applications of an infrared Doppler lidar in detection of wind shear. *J. Atmos. Oceanic Technol.*, **25**, 637–655.
- , S. Y. Lau, and O. S. M. Lee, 2003: Terminal Doppler weather radar observation of atmospheric flow over complex terrain during tropical cyclone passages. *J. Appl. Meteor.*, **42**, 1697–1710.
- Sun, J., D. Flicker, and D. Lilly, 1991: Recovery of three dimensional wind and temperature fields from simulated Doppler radar data. *J. Atmos. Sci.*, **48**, 876–890.
- Tang, W., P. W. Chan, and G. Haller, 2010a: Accurate extraction of Lagrangian coherent structures over finite domains with application to flight data analysis over Hong Kong International Airport. *Chaos*, **20**, 017502, doi:10.1063/1.3276061.
- , M. Mathur, G. Haller, D. C. Hahn, and F. H. Ruggiero, 2010b: Lagrangian coherent structures near a subtropical jet stream. *J. Atmos. Sci.*, **67**, 2307–2319.

Copyright of Journal of Applied Meteorology & Climatology is the property of American Meteorological Society and its content may not be copied or emailed to multiple sites or posted to a listserv without the copyright holder's express written permission. However, users may print, download, or email articles for individual use.